RSC Advances

ROYAL SOCIETY OF CHEMISTRY

www.rsc.org/advances

NO_x storage and soot combustion over well-dispersed mesoporous mixed oxides via hydrotalcite-like precursors

Zhongpeng Wang [a,*], Peng Lu [a], Xiaomin Zhang [a], Liguo Wang [a], Qian Li [b], Zhaoliang Zhang [b]

[a] *School of Resources and Environment, University of Jinan, 106 Jiwei Road, Jinan 250022, P R China*

[b] *College of Chemistry and Chemical Engineering, University of Jinan, 106 Jiwei Road, Jinan 250022, P R China*

* Corresponding author:

Dr. Zhongpeng Wang, Professor

School of Resources and Environment, University of Jinan,

106 Jiwei Road, Jinan 250022, P. R. China;

E-mail: chm_ wangzp@ujn.edu.cn;

Tel/Fax: +86 531 82769233

Abstract: A series of mixed oxides with highly dispersed redox components were prepared via hydrotalcite-like precursors in which Mg was partly substituted with copper and cobalt, which were employed for NOx storage and soot combustion. The physico-chemical properties of the catalysts were characterized by XRD, TGA, IR, N_2 adsorption, H_2-TPR and *in situ* FTIR techniques. The results shows the transition metal cations have isomorphously replaced Mg^{2+} in the layered structures forming a single hydrotalcite type phase. After calcinations, the transition metal oxides exist as highly dispersed form in the Mg(Al)O matrix and there is a cooperative effect between the copper and cobalt on redox property of the catalyst. The as-prepared oxides catalysts exhibit large surface areas, basic characters and improved redox properties, resulting in high performances on NOx storage and soot combustion. Both the NOx storage and desorption are catalytically accelerated due to the highly dispersed transition metal oxides. The presence of NOx positively affects the activity of all the oxides catalysts for soot combustion, which may be related to the production of NO_2 during NO oxidation. NO_2-assisted mechanism and active oxygen mechanism may occur simultaneously in soot/NO/O_2 reaction.

Keywords: catalytic activity; NOx storage; soot combustion; hydrotalcite; cobalt/copper

1. Introduction

Diesel engines with excellent fuel economy are receiving much attention as an effective method of reducing CO_2 emission to suppress global warming. However on the other hand, suppression of diesel emissions is the major issue from the aspect of improving urban environment. Nitrogen oxides (NOx) and soot particulates (PM) are considered to be the main pollutants emitted from diesel engines together with CO and HC causing serious problems to global environment and human health[1]. Emissions of HC and CO are low and can be easily oxidized to CO_2 by diesel oxidation catalysts (DOC). As fuel processing and engine design modifications alone will not meet the

stringent legislations for both NOx and soot, the after-treatment technologies for the removal of NOx and soot are quite necessary.

For soot removal, filtration and controllable regeneration within the exhaust stream are among the most promising methods, while the key technology is oxidation catalysis[2, 3]. In the past few decades, many materials have been applied in oxidation catalysis, with transition-metal oxides[4-6], alkaline metal oxides[7-10], perovskite-like type oxides[11, 12], noble metals[3, 13] and ceria-based oxides[14-18] being the outnumbering materials. However, a cheap and efficient substitute with low-temperature activity and high selectivity is still desired. In spite of several drawbacks, there are now commercially available after-treatment technologies such as catalyzed soot filter (CSF)[19], continuously regenerating trap (CRT)[20] and fuel borne additives (FBC), for decreasing soot emissions from various sources.

For the control of NOx emissions, the NH_3/Urea selective catalytic reduction (SCR)[21] and the NOx storage-reduction (NSR)[22], also called as lean NOx trap (LNT), are widely accepted as the most hopeful strategies. The Urea-SCR has a high NOx purification rate but has been essentially developed for heavy-duty trucks and buses due to deficiencies in the infrastructure with respect to urea supply. Meanwhile, a more confusing context characterizes light vehicles with a competition between SCR and NSR after-treatment systems. The mechanism of NSR catalyst is that the exhaust NOx in lean conditions is stored on the catalyst surface, and the stored NOx is reduced in rich conditions when the exhaust gas does not contain any oxygen. Both technologies suffer from strong kinetic and thermodynamic limitations, which make a suitable solution difficult. In addition, the main challenge is the reduction of the catalyst volume and the automatic control of urea injection in the particular case of urea SCR systems[23].

Considering the pollutants emitted from diesel engines as a whole, the most feasible removal method is the integration of NOx traps and oxidation catalysts[24]. Based on this concept, the Toyota group has developed a practical catalyst system (Diesel Particulate-NOx Reduction System: DPNR)

[25]that is a world first simultaneously reduction system of PM and NOx-a task that was previously considered impossible. The DPNR system has been applied to the diesel engine-powered light-duty trucks (Toyota Dyna, Hino Dutro) in Japan, and to a passenger vehicle (Toyota Avensis) in Europe. Similar with the NSR catalytic material (e.g., Pt-Ba/Al_2O_3 or Pt-K/Al_2O_3), DPNR catalysts work under cyclic conditions alternating a lean phase during which NOx in the exhausts are stored as nitrates with a short rich phase, during which the stored NOx are reduced to nitrogen. During these cycles, soot removal occurs as well through oxidation by active oxygen species generated in both the NOx storage and reduction processes, together by excessive oxygen under lean conditions.

So far, many kinds of metal oxides catalysts have been investigated as NOx traps and oxidation catalysts, such as Pt-Ba/Al_2O_3[26], Pt-K/Al_2O_3[27], K/La_2O_3[28], Ba,K/CeO_2[29] and perovskites catalysts[30, 31], etc. For several years, Mg-Al hydrotalcite mixed oxides[22, 32-34] were reported to offer potential advantages over Pt/BaO/Al_2O_3 in NOx storage-reduction and assessed to be the new generation of NSR catalysts. In our previous studies[6, 35-38], hydrotalcites-derived oxides catalysts containing noble metals, transition metals or rare earth metals are catalytically active for NOx storage, soot oxidation, and NOx reduction by soot. In addition, Meng et al.[39-41] also reported a series of hydrotalcites-related oxides exhibited similar multifunctional activity for diesel soot and NOx abatements. Hydrotalcites compounds can contain metal cations of more than two types, which provide a good platform for design of catalysts combining redox and basic properties. After calcinations at high temperatures, the derived oxides catalyst presents large surface areas, redox and basic properties, high metal dispersions and good thermal stability, which is promising to be one novel DPNR catalytic material.

With regard to the noble metal-free catalysts derived from hydrotalcites, transition metal oxides with bulk or spinel structure have attracted much attention as catalysts or catalyst supports for soot oxidation and NOx storage because of the enhanced redox properties. In contrast, transition metal oxides with highly dispersed form draw a few interests. In fact, hydrotalcites-derived Mg/Al mixed oxide can act simultaneously as support for the dispersed metals with redox properties and as NOx

storage component. It is also known that the surface properties of the redox component and the storage component are critical to the efficacy of the NOx storage-redction catalysts. Motivated by the above considerations, a series of mixed oxides with highly dispersed redox components were prepared via hydrotalcite-like precursors in which Mg was partially substituted with copper and cobalt. The as-prepared oxides catalyst exhibited high performances on NOx storage and soot combustion, which were discussed with their high surface areas, porous structures and improved redox properties.

2. Experimental

2.1 Catalyst preparation

The hydrotalcites precursors with different metal atomic ratio listed in Table 1 were prepared by co-precipitation of an aqueous solution of suitable metal nitrates (the molar ratio M^{2+}/M^{3+} was 3) with an aqueous solution of 2 M NaOH and 1 M Na_2CO_3. The two solutions were mixed under vigorous stirring at 25 ºC with the pH maintained constant at 10.0±0.5. The resulting slurry was aged in the mother liquor at 80 ºC for 1 h. It was then filtered off and repeatedly washed with sufficient deionized water to ensure that the sodium content in the solid was lower than 0.05 wt.%. The precipitate was then dried at 120 ºC for 12 h to obtain hydrotalcites precursors. Samples are denoted according to the metal constituents in the initial mixture. $Mg_{75}Al_{25}$-HT, $Cu_5Mg_{70}Al_{25}$-HT, $Co_5Mg_{70}Al_{25}$-HT and $Cu_5Co_5Mg_{65}Al_{25}$-HT (marked as HT, CuHT, CoHT and CuCoHT, respectively) were similarly prepared.

The corresponding mixed oxides were obtained by thermal decomposition of hydrotalcites precursors at 800 ºC in air for 4 h, referred as to MgAl, CuMgAl, CoMgAl and CuCoMgAl, respectively.

2.2 Catalyst characterization

XRD was conducted with a BRUKER-AXS D8Adance X-Ray Diffractometer using Cu Kα radiation, at 40 KV and 40 mA, in the scanning angle (2θ) range of 5°~80° at a scanning speed of 3 °/min.

Thermogravimetric analysis was carried out using METTLER TOLEDO TGA/DSC1, with air as carrier gas (30 ml/min) at a heating rate of 10 ºC/min from 35 to 900 ºC.

Texture properties of the prepared samples were determined from N_2 adsorption-desorption isotherms performed using a Micromeritics ASAP 2020 surface area analyzer after outgassing at 300 ^{o}C for 5 h prior to analysis. The specific surface areas were calculated with the Brunauer-Emmett-Teller (BET) equation on the basis of the adsorption data. Pore size distribution over the mesopore range was generated by the Barrett-Joyner-Halenda (BJH) analysis of the desorption branches, and values of the average pore size were calculated.

Infrared spectra were recorded on a Bruker Tensor 27 spectrometer over 400–4000 cm^{-1} after 32 scans at a resolution of 4 cm^{-1}. The samples were prepared in the form of pressed wafers (2% of sample in KBr).

Temperature-programmed reduction with H_2 (H_2-TPR) experiments were performed in a quartz reactor with a thermal conductivity detector (TCD) to monitor the H_2 consumed. A 50 mg sample was pretreated *in situ* at 500 °C for 1 h in a flow of O_2 and cooled to room temperature in the presence of O_2. TPR was conducted at 10 °C/min up to 900 °C in a 30 ml/min flow of 5 vol. % H_2 in N_2.

2.3 NOx adsorption and desorption experiments

The NOx storage performance was studied by isothermal adsorption of NOx followed by temperature programmed desorption (TPD) of adsorbed species. The catalysts were finely ground, sized in 40-80 mesh for NO_x adsorption/desorption experiments. Thermal NO_x adsorption experiments were carried out in a quartz flow reactor (i.d. = 6 mm and L = 240 mm) using 50 mg of the catalysts. Catalyst was pretreated *in situ* at 500 ºC for 1 h in N_2 and then cooled to 100 ºC. When

the temperature had stabilized at 100 ºC, the flow gas was switched to 1050 ppm NO and 5% O_2 in He at a rate of 100 mL/min for 60 min for thermal NO_x adsorption. Concentration of NO, NO_2 and NO_x from the reactor outlet were monitored by a chemiluminiscence NO_x analyzer (Model 42i-HL, Thermo Electron Corporation).

After the isothermal NO_x adsorption, the flow gas was switched to pure N_2 (rate = 100 mL/min) to flush the catalysts until NO_x is not detected. The NOx-TPD was conducted by heating the catalysts from 100 ºC to 700 ºC at a heating rate of 10 ºC/min with N_2 flowing at a rate of 100 mL/min. Concentrations of NO, NO_2 and NO_x from the reactor outlet were monitored by the chemiluminiscence NO_x analyzer, and the desorbed NO_x amount was thus calculated as the NOx storage capacity of the catalyst.

2.4 *In situ* FTIR study of NOx storage

The *in situ* FTIR spectra were recorded on a Bruker Tensor 27 spectrometer over 400–4000 cm^{-1} after 32 scans at a resolution of 4 cm^{-1}. The self-supporting wafers of the oxide catalyst were loaded into an *in situ* infrared transmission cell which is capable of operating up to 500 °C and equipped with gas flow system. The wafers were pretreated in the IR cell at 400 °C in a flow of He for 30 min to remove any adsorbed species. After cooled to 100 °C, the background spectrum was recorded. The time-resolved IR spectra were recorded at 100 °C in the flow of 1000 ppm NO + 5 vol.% O_2 in He (100 mL/min).

2.5 Catalyzed NO oxidation into NO_2

NO oxidation on the catalysts was investigated by a temperature-programmed oxidation (TPO) technique in the same experimental apparatus as used in NOx storage experiments. The catalysts (40-80 mesh, 50 mg) were pretreated *in situ* at 500 °C for 1 h in He. After cooled down to room temperature, a feed gas containing 1000 ppm NO + 5 vol.% O_2 in He (100 ml/min) was introduced and NOx oxidation was started at a heating rate of 4 °C/min until 700 °C. Concentrations of NO, NO_2 and NO_x from the reactor outlet were monitored by a chemiluminiscence NO_x analyzer.

2.6 Catalytic combustion of soot

The model soot used in this study was Printex-U from Degussa with surface area of 93.5 m^2/g. The mean agglomerate size measured using a Beckman Counter LS13320 laser particle size analyzer was about 177 nm[9].

The catalytic reactions for soot combustion were performed by a TPO technique in a fixed-bed flow reactor as described in our previous works[36, 38, 42]. Briefly, the soot was mixed with the catalyst in a weight ratio of 1:9 in an agate mortar for 10 min, which results in a tight contact. A 50 mg sample of the soot/catalyst mixture was pretreated in He (100 ml/min) at 200 °C for 1 h to remove surface-adsorbed species. After cooling down to room temperature, a gas flow with 5 vol. % O_2 in He or 1000 ppm NO + 5 vol. % O_2 in He (100 ml/min) was introduced and then TPO was started at a heating rate of 10 °C/min until 800 °C. NOx (NO and NO_2) and COx (CO and CO_2) in the effluent were online analyzed by the chemiluminiscence NOx analyser (42i-HL, Thermo Environmental) and a gas chromatograph (GC) (SP-6890, Shandong Lunan Ruihong Chemical Instrument Corporation, China), respectively. The characteristic temperatures from the TPO profiles, T_5 and T_{50} are defined as the temperatures at which 5% and 50% of the soot is converted, respectively. The selectivity to CO_2 formation (S_{CO2}) is defined as the percentage outlet CO_2 concentration divided by the sum concentrations of the outlet CO_2 and CO. NOx conversion is evaluated by maximum NOx conversion (C_m) during each TPO process as described in our previous works.

3. Results and discussion

3.1 XRD analysis

Fig. 1 depicts the powder XRD patterns of the hydrotalcites precursors and their derived mixed oxides whilst Table 1 summarizes the chemical composition and relevant structural parameters. As shown in Fig.1a, all the as-prepared precursors show sharp and symmetric reflections at lower 2θ values of 11.5° (003), 21.5° (006) and 34.5° (009), which are characteristic diffraction patterns of hydrotalcite with layered structures (JCPDS no. 22-0700). The well defined (110) and (113)

diffraction peaks at 60.3° and 61.5° reveal a quite good dispersion of metal ions in the brucite-like layers[43]. No other phases were detected after transition metals incorporation, which suggests that magnesium and aluminum may be substituted by copper or cobalt in the brucite-like layers.

The lattice parameters, *a* and *c*, typical of hydrotalcite structures with rhombohedral 3R symmetry were calculated for all samples and listed in Table 1. The ''*a*'' parameter corresponds to the average distance cation–cation in the layers of brucite type, which is obtained by a = 2 *d*(110). The ''*a*'' values are slightly increased after transition metals incorporation, which is in agreement with other research[44]. This is due to Mg^{2+} substitution by a larger cations Co^{2+} and Cu^{2+}(rCo^{2+} = 0.74 Å, rCu^{2+} = 0.69 Å , rMg^{2+} = 0.65 Å), and suggests the formation of a single hydrotalcite type phase. In the case of ''*c*'' parameter, it is related to the thickness of the layer brucite type and interlayer distance, which is usually calculated using the relationship c = 3 *d*(003). It depends upon several factors such as the amount of interlayer water, the size of the interlayer anion and of the M^{2+}-M^{3+} cations, and the strength of the electrostatic attractive forces between the layer and the interlayer[45]. The results shown in Table 1 must probably reflect the influence of these various factors.

The full width at half maximum (FWHM) of the (003) plane ($2\theta \approx 11.5°$) is included in Table 1 as a measure of crystallinity of the hydrotalcite phase in the *c*-axis direction. The FWHM value increases after Cu or/and Co doped, demonstrating that the crystallinity of the HT phase decreases due to the distortion induced by the dopants. The average crystallite size calculated from *d*(003) and *d*(110) planes using Debye-Scherrer equation varied in the range 80-100 Å.

As shown in Fig. 1b, the hydrotalcite phases were completely destroyed and new oxide derivatives were formed after calcination at 800 °C. For all calcined samples, three peaks with the 2θ angle centered at 36.9°, 42.9° and 62.3° were ascribed to the periclase-type MgO (JCPDS 45-0946, marked with #) with traces amount of spinel-type $MgAl_2O_4$ (JCPDS 47-0254, marked with o) at 2θ=35.5°. Contrarily as it occurs with the calcined Cu- and Co-hydrotalcites[42, 46], no peaks assigned to the

transition metal oxide were observed, indicating that the copper or cobalt oxides are well dispersed in the Mg(Al)O matrix[45].

3.2 Thermal gravimetric analysis (TGA and DTG)

Fig. 2 presents the weight loss rates of the precursors as a function of temperature during heating in air, revealing the transformation of hydrotalcites into the corresponding oxides. Generally, a similar thermal behavior was observed on the four prepared precursors which exhibit a two-stage thermal decomposition with a total mass loss of ~45% as summarized in Table 1. Considering that the interlayer anions in the hydrotalcites precursors are carbonates through FTIR spectra (not shown here), the first stage occurred at 100-250 ºC was ascribed to the release of interlayer and adsorbed water molecules with weight loss of 15.8-17.7%. The second stage of the weight loss (~28%) at 250-500 ºC consists of dehydroxylation of interlayer hydroxyl groups and decomposition of interlayer carbonate and traced nitrate, resulting in the collapse of the layered structure. After small amounts of Cu and/or Co introduced into hydrotalcite structure, the second weight loss shifts to low temperature range. The accelerated decomposition can be attributed to distortion of brucite-like sheets modified by substitution of Mg and Al cations by transition metals, resulting in weakening of anions bounding by hydrotalcite layers[44].

3.3 Textural characteristics

The textural properties of the mixed oxides obtained by nitrogen adsorption at -196 °C, are summarized in Table 2. The specific surface area reaching 186 m^2/g for the MgAl mixed oxide, decreased slightly upon introduction of the transition metal cations in the structure being in the range 166−185 m^2/g. Such a reduction in the surface area may be related to the aggregation of metallic oxides blocking the smaller pores and/or causing some structural rearrangements[47].

N_2 adsorption and desorption isotherms of MgAl, CuMgAl, CoMgAl and CuCoMgAl mixed oxides are plotted in Fig. 3. All the samples displayed type IV nitrogen adsorption/desorption isotherms (according to IUPAC classification) with a distinct hysteresis loop, characteristic of

mesoporous materials. The hysteresis loop is ascribed to H3 type, which is usually given by adsorbents containing slit-shaped pores with a wide distribution of pore size. Applying the BJH method to the isotherm desorption branch, average pore size of 21 nm or smaller is assigned to the mixed oxides.

The pore size distribution curves for the mixed oxides are plotted in the insets in Fig. 3, which display that most of the pores fall in meso size range (2 nm<r_p<50 nm). The pores present in the mixed oxides exhibit monomodal curves with the maximum at ≈11 nm, favoring gas molecule diffusion in the pores and thus ruling out the diffusion limitation in the adsorption and desorption process[48].

3.4 H_2-TPR

H_2-TPR was used to examine the redox properties of catalysts. Fig. 4 presents TPR profiles for mixed oxides catalysts. Differences in the redox properties for these samples can be anticipated to the nature of the transition metal and the crystal phases present in the compounds. For MgAl sample, no reduction of magnesium or aluminum species is observed until 800 ºC, as expected. In the case of CoMgAl, the reduction proceeds largely in two stages. The first reduction zone with weak and broad peak from 200 to 450 ºC corresponds to the reduction of Co_3O_4 into Co^0 ($Co_3O_4 \rightarrow CoO \rightarrow Co$), while the second peak at above 600 ºC is attributed to the reduction of $CoAl_2O_4$ to Co^0 [49, 50]. Concerning CuMgAl solid, a sharp peak centered at 233 ºC was detected, which can be ascribed to the reduction of the highly dispersed copper oxides species, including isolated copper ions, weak magnetic associates, and small two- and three-dimensional clusters[51]. As well documented[38, 52, 53], bulk CuO gave TPR signals at much higher temperatures (~ 300 ºC) than highly dispersed CuO species. Since such signals are absent in our TPR spectra, we can exclude the presence of bulk like CuO species, which is in consistent with XRD results. As for the CuCoMgAl sample, two reduction peaks were found at different temperatures. The first peak assigned to the highly dispersed CuO and Co_3O_4 species, while the seond peak at above 550 ºC is attributed to the reduction of $CoAl_2O_4$. It can be

seen from Fig. 4 and Table 2 that the first reduction peak becomes shaper and shifts to lower temperature (225 ºC) with a higher H_2 consumption compared with that of CuMgAl. The promoting effect of Cu-Co incorporation on reducibility at low temperature may be associated with the increase of the interaction among transition metal ions in the Mg(Al)O matrix. Evidence of a strong interaction between copper and cobalt in the mixed oxides catalysts have been given in investigation of Co*x*O*y*–CuO mixed oxides[54].

These TPR results together with those described previously by XRD show that transition metal oxide exist as highly dispersed form in the matrix and there is a cooperative effect between the copper and cobalt on reducibility of the catalyst. Such a cooperative effect is very likely originated by the intimate contact and by the good interdispersion of the different oxides forming the catalyst via hydrotalcites precursors.

3.5 NO oxidation

NO_2 is considered as an important intermediate in both NOx storage and soot oxidation. NOx storage materials are generally more effective in adsorbing NO_2 than NO, and NO_2 formation is a beneficial precursor step to adsorption. Besides, NO_2 has also been proved to be a more powerful oxidant for soot oxidation than NO and O_2. Soot-trapping followed by oxidation with the highly reactive NO_2 is the basis of the so-called Continuously Regenerating Trap (CRT) which is already a commercialized technology for decreasing particulate emissions from various sources. Fig. 5 shows the NO_2 formation profiles in the catalyzed NO oxidation reactions. It should be noted that in the absence of catalyst less than 3% of NO is oxidized to NO_2 because of the effect of temperature[55]. As can be seen from Fig. 5, NO can be readily oxidized to NO_2 on all catalysts even at low temperature with about 10% of NO converted at 100 ºC. When the temperature exceeds 300 ºC, the transition metal-containing catalysts accelerate the oxidation of NO with a maximum NO_2 level at 400-450 ºC while MgAl does not present such behavior under the same conditions and only a weak and broad

peak was observed at ~550 ºC. Above the maximum the NO_2 level decreases following the thermodynamic profile of the NO/NO_2 equilibrium. From the maximum NO_2 level in the TPO profiles the NO_2 production capacity decreases by the following order: CuCoMgAl > CuMgAl > CoMgAl > MgAl, which is in line with the reducibility of the catalysts. Sufficient NO_2 production capacity is needed in NOx storage and NO_2-assisted soot oxidation.

3.6 NOx storage and in situ FTIR spectra

NOx storage experiment was carried out by isothermal adsorption of NO in the presence of O_2 at 100 ºC over the hydrotalcites-derived mixed oxides. The stored NOx species were investigated by in situ FTIR spectra as a function of time shown in Fig. 6. At low contact time, on MgAl sample ionic nitrite (bands at 1226 cm^{-1}) and bridged bidentate nitrite (bands at 1278 cm^{-1}) due to the adsorption of NO are simultaneously present with bridged bidentate nitrate (bands at 1675-1631 cm^{-1}, bands at 1310 cm^{-1}) attributed to NO_2 adsorption. On increasing the adsorption time, the bands due to ionic nitrite and bridged bidentate nitrite progressively increased in intensity, whereas those of bidentate nitrate grew slowly. The simultaneous presence of nitrite and nitrate leads to the overlapped peak of ionic nitrite with bridged bidentate nitrate at 1310 cm^{-1}. After 40 min of contact, the adsorption of NOx reached saturation with nitrites as the predominant species on the Mg-Al sites.

For CuMgAl sample, bridged bidentate nitrate (bands at 1310 cm^{-1} and 1675-1631 cm^{-1}) and monodentate nitrate (1275 cm^{-1}) were formed in the NOx adsorption at 100 ºC, besides ionic nitrite (bands at 1219 cm^{-1}). The time-dependent spectra (Fig. 6 b) clearly show that the increase in nitrate peak occurs simultaneously with the decrease of ionic nitrite bands, suggesting a redox conversion from ionic nitrite to nitrate species in the presence of well dispersed copper oxide. Similar results were observed on NOx adsorption over CoMgAl and CuCoMgAl. Compared with MgAl sample, more nitrates together with ionic nitrite are the major NOx species stored over the transition metal-containing mixed oxides. Thus, NOx adsorption at low temperatures was enhanced due to the conversion of nitrites into nitrates on the highly dispersed Cu/Co oxides, which are then stored on the

adjacent Mg-Al sites to form relatively stable Mg/Al nitrates and nitrites. Taking into account the above-mentioned NO oxidation results and the previous reports[37, 48, 56], NO can be stored on Cu and/or Co incorporated hydrotalcite catalysts by two different pathways in the presence of O_2: (1) the NO oxidation to nitrites followed by oxidation to nitrates; (2) the NO oxidation to NO_2 followed by adsorption as nitrates. Both the two routes are promoted by the highly dispersed transition metal oxides species.

3.7 NOx desorption from mixed oxide catalysts

Fig. 7 presents the desorption profiles of NOx at 100-600 ºC from the oxides catalysts after NOx adsorption at 100 ºC. The desorbed amounts of NOx were calculated as the NOx storage capacity and listed in Table 2. In general, the NOx desorption follows a two-step process in which NO is the predominant species, with a small amount of NO_2 (less than 30 ppm over 100-600 ºC). Thus, the decomposition of surface nitrates and nitrites tends to undergo the following reactions:

$$4NO_3^- \rightarrow 4NO+3O_2+2O^{2-}{}_{(s)}$$

$$4NO_2^- \rightarrow 4NO+O_2+2O^{2-}{}_{(s)}$$

Besides gaseous NO and O_2, a large amounts of basic oxygen ions were also formed on the catalyst surface during the desorption process.

For MgAl sample, the low temperature desorption exhibits a broak peak at 320 ºC corresponding to various types of nitrites while the weak desorption at high temperature (520 ºC) is related to various nitrates, which is consistent with the IR results. After Cu and/or Co incorporated, the two steps occurred at much lower temperatures and over a much narrower temperature range, presumably because of the catalytic activity of copper and /or cobalt for NOx desorption. Obviously, the desorption peaks at both low and high temperature on transition metal-containing oxides are larger than those on MgAl sample, resulting in enhanced NOx storage capacity. From the calibrated areas of the TPD peaks, a rather high NOx storage capacity at 100 ºC (5.20 mg/g) was observed on CoMgAl solid.

It can be seen from the in situ FTIR spectra and NOx desorption results that both the storage and desorption are catalytically accelerated due to the highly dispersed transition metal oxides. It is suggested[57] that higher NOx adsorption is due to a migration process of NO_3^- and NO_2^- from surface active metal oxides to adjacent Mg-Al sites to form relatively stable Mg/Al nitrates and nitrites. Thus, the role of well dispersed Cu or/and Co oxides in NOx storage and decomposition in the present study may be similar to the noble metal (Pt) in Toyota NSR catalysts[58].

3.8 Soot oxidation with O_2 and NO + O_2

The soot conversion profiles obtained during catalytic tests performed CO_2 with O_2 and NO+O_2 are plotted as a function of temperature in Fig. 8, including the curves obtained with catalyst-soot mixture and SiO_2-soot mixture. The derived parameters of T_5, T_{50} and S_{CO2} under different conditions are summarized in Table 3.

As shown in Fig. 8 (a), the blank experiment with O_2 was performed mixing the soot with SiO_2, and the ignition temperature was 470 ºC. In comparison with the non-catalyzed soot oxidation, soot conversion curves over the mixed oxides shift to lower temperature range with T_5 and T_{50} decreased. MgAl sample exhibits modest activity with a shift of T_5 by 48 ºC to lower temperature. After transition metals introduced, the soot oxidation activity was improved whilst the selectivity to CO_2 formation was increased to 100%, which may be related to the enhancement of reducibility of the catalysts as mentioned in TPR results. CuMgAl and CuCoMgAl show better catalytic performances with similar ignition temperatures at about 315 ºC under the feed gas of O_2. Considering that the reducible oxygen species of CuMgAl measured in terms of TPR were less than that of CuCoMgAl, the accessible oxygen species was not the sole determining factor for the catalytic oxidation of soot, which has also been approved by isotopic TPO investigations on catalytic soot oxidation[59, 60]. Also worth noting is the well dispersed transition metal oxides catalysts exhibit higher ignition activity than the bulk copper or coboalt oxides samples[6, 38] derived from hydrotalcites under the same

conditions, which could be ascribed to the improved reducibility, larger surface areas and pore volumes of the former.

It can be seen from Fig. 8(b) and Table 3 that the presence of NO positively affects the activity of all the oxides catalysts over the entire soot conversion range. Moreover, the Cu/Co incorporated catalysts also show improved activity for NOx removal, with the largest *Cm* (maximum conversion of NOx) of about 30% obtained over CuMgAl sample. The promotion effect of NO on soot combustion at low temperature is more obvious on MgAl with T_5 decreased from 422 to 320 ºC, compared with transition metal incorporated samples. Interestingly, a bimodal CO_2 formation curve was observed on MgAl sample with a minor CO_2 peak at about 360 ºC and a larger one centered at 570 ºC. The two peaks profile of the TPO results in NO+O_2 were also reported in our previous work [36, 61], which suggests that the first peak in the low temperature range corresponds to the reaction of carbon with NO_2, whereas at higher temperatures oxidation with O_2 is dominating. Interestingly, MgAl catalyst shows higher ignition activity (value of T_5), namely lower combustion temperature (around 300 ºC) in NO+O_2 than that of CoMgAl catalyst, which can be ascribed to its higher NO_2 production at the same temperature range. The promotion effect of Cu and/or Co incorporation are manifested by the disappearance of higher temperature combustion peak with lower T_{50} and soot depletion below 500 ºC. Similarly, CuMgAl and CuCoMgAl also show close ignition performance with T_5 of about 300 ºC, while CuCoMgAl exhibits lower T_{50} value of 467 ºC implying a cooperative effect between the copper and cobalt in the mixed oxides.

With regard to the promotion effect of NOx adsorbed species on soot oxidation, the catalytic activity for soot oxidation in NO+O_2 seems to be related to the production of NO_2, which is a stronger oxidant than NO and O_2. In Fig. 9, the temperature at which 50% of the soot is converted (T_{50}) in catalytic tests has been plotted as a function of maximum level of NO_2 reached by each catalyst in the catalyzed NO oxidation reactions. Obviously, the most active catalyst (CuCoMgAl) in terms of T_{50} is also the most effective for NO conversion to NO_2 and vice versa. An approximate

linear relationship between the soot combustion and NO_2 production has been obtained, which demonstrates that the combustion of soot over the hydrotalcites-derived Cu/Co oxides catalysts mainly occurs through the NO_2-assisted mechanism. A similar relationship was also obtained previously with a set of ceria catalysts[15]. Taking into account the mechanism for soot combustion on K/MgAlO oxides in our previous works[35, 36, 62], the catalytic combustion of soot under $NO+O_2$ on well dispersed transition metal oxides catalysts may be initiated by the attack of NO_2 to the soot surface, and once the soot surface is partially oxidized and the temperature is high enough, some other oxidizing species such as molecular O_2, surface nitrates/nitrites or active oxygen species released by Cu/Co oxides, are also able to oxidize soot along with NO_2. Thus, two different reaction mechanisms, active oxygen mechanism and NO_2-assisted mechanism, may occur simultaneously on the soot/NO/O_2 reaction in the present study.

4 Conclusions

In the present study, a series of mixed oxides with redox components were prepared via hydrotalcite-like precursors in which a small amount of Mg was substituted with copper and cobalt. The transition metal oxides exist as highly dispersed form in the matrix and there is a cooperative effect between the copper and cobalt on reducibility of the catalyst. The as-prepared oxides catalysts exhibit large surface areas, basic characters and improved redox properties, resulting in high performances on NOx storage and soot combustion. Both the NOx storage and desorption are catalytically accelerated due to the highly dispersed transition metal oxides. The presence of NO positively affects the catalytic activity for soot oxidation, in which NO_2-assisted mechanism and active oxygen mechanism may occur simultaneously.

Acknowledgements

This work was financially supported by the National Natural Science Foundation of China (No. 21007019 and 21277059), the Development Program of the Science and Technology of Shandong

Province (No. 2014GSF117039), Jinan Science and Technology Development Plan (No. 201303066), and National Science & Technology Pillar Program (2014BAK13B02).

References

1. S. Menon, J. Hansen, L. Nazarenko and Y. Luo, *Science*, 2002, **297**, 2250-2253.
2. J. P. A. Neeft, M. Makkee and J. A. Moulijn, *Appl. Catal. B*, 1996, **8**, 57-78.
3. Y. Wei, J. Liu, Z. Zhao, Y. Chen, C. Xu, A. Duan, G. Jiang and H. He, *Angew. Chem. Int. Edit.*, 2011, **50**, 2326-2329.
4. F. E. López-Suárez, A. Bueno-López, M. J. Illán-Gómez, A. Adamski, B. Ura and J. Trawczynski, *Environ. Sci. Technol.*, 2008, **42**, 7670-7675.
5. D. Reichert, H. Bockhorn and S. Kureti, *Appl. Catal. B*, 2008, **80**, 248-259.
6. Z. Wang, X. Zhang, L. Wang, Z. Zhang, Z. Jiang, T. Xiao, A. Umar and Q. Wang, *Sci. Adv. Mater.*, 2013, **5**, 1449-1457.
7. R. Kimura, J. Wakabayashi, S. P. Elangovan, M. Ogura and T. Okubo, *J. Am. Chem. Soc.*, 2008, **130**, 12844-12845.
8. N. A. Comelli, M. L. Ruiz, N. A. Merino, I. D. Lick, E. Rodriguez-Castellon, A. Jimenez-Lopez and M. I. Ponzi, *Appl. Clay Sci.*, 2013, **80-81**, 426-432.
9. Z. Zhang, Y. Zhang, Z. Wang and X. Gao, *J. Catal.*, 2010, **271**, 12-21.
10. M. E. Gálvez, S. Ascaso, I. Tobías, R. Moliner and M. J. Lázaro, *Catal. Today*, 2012, **191**, 96-105.
11. Y. Teraoka, K. Nakano, S. Kagawa and W. F. Shangguan, *Appl. Catal. B*, 1995, **5**, L181-L185.
12. X. Wang, Y. Zhang, Q. Li, Z. Wang and Z. Zhang, *Catal. Sci. Technol.*, 2012, **2**, 1822-1824.
13. J. Oi-Uchisawa, S. Wang, T. Nanba, A. Ohi and A. Obuchi, *Appl. Catal. B*, 2003, **44**, 207-215.
14. E. Aneggi, D. Wiater, C. de Leitenburg, J. Llorca and A. Trovarelli, *ACS Catal.*, 2013, **4**, 172-181.
15. A. Bueno-Lopez, *Appl. Catal. B*, 2014, **146**, 1-11.
16. J. Liu, Z. Zhao, J. Wang, C. Xu, A. Duan, G. Jiang and Q. Yang, *Appl. Catal. B*, 2008, **84**, 185-195.
17. H. Zhang, F. Gu, Q. Liu, J. Gao, L. Jia, T. Zhu, Y. Chen, Z. Zhong and F. Su, *RSC Adv.*, 2014, **4**, 14879-14889.
18. Q. Yang, F. Gu, Y. Tang, H. Zhang, Q. Liu, Z. Zhong and F. Su, *RSC Adv.*, 2015, **5**, 26815-26822.
19. B. C. Choi and D. E. Foster, *J. Mech. Sci. Technol.*, 2006, **20**, 1-12.
20. A. Setiabudi, M. Makkee and J. A. Moulijn, *Appl. Catal. B*, 2004, **50**, 185-194.
21. P. Li, Y. Xin, Q. Li, Z. Wang, Z. Zhang and L. Zheng, *Environ. Sci. Technol.*, 2012, **46**, 9600-9605.
22. M. Jabłońska, A. E. Palomares and L. Chmielarz, *Chem. Eng. J.*, 2013, **231**, 273-280.
23. P. Granger and V. I. Parvulescu, *Chem. Rev.*, 2011, **111**, 3155-3207.
24. V. G. Milt, E. D. Banus, M. A. Ulla and E. E. Miro, *Catal. Today*, 2008, **133-135**, 435-440.
25. J. Suzuki and S. Matsumoto, *Top. Catal.*, 2004, **28**, 171-176.
26. N. Artioli, R. Matarrese, L. Castoldi, L. Lietti and P. Forzatti, *Catal. Today*, 2011, **169**, 36-44.
27. R. Matarrese, L. Castoldi, N. Artioli, E. Finocchio, G. Busca and L. Lietti, *Appl. Catal. B*, 2014, **144**, 783-791.
28. V. G. Milt, M. L. Pissarello, E. E. Miro and C. A. Querini, *Appl. Catal. B*, 2003, **41**, 397-414.
29. M. A. Peralta, V. G. Milt, L. M. Cornaglia and C. A. Querini, *J. Catal.*, 2006, **242**, 118-130.
30. V. G. Milt, M. A. Ulla and E. E. Miro, *Appl. Catal. B*, 2005, **57**, 13-21.
31. Z. Li, M. Meng, Y. Zha, F. Dai, T. Hu, Y. Xie and J. Zhang, *Appl. Catal. B*, 2012, **121–122**, 65-74.
32. F. Basile, G. Fornasari, M. Livi, F. Tinti, F. Trifiro and A. Vaccari, *Top. Catal.*, 2004, **30-31**, 223-227.
33. J. J. Yu, X. P. Wang, L. D. Li, Z. P. Hao, Z. P. Xu and G. Q. M. Lu, *Adv. Funct. Mater.*, 2007, **17**, 3598-3606.
34. S. J. Park, H. A. Ahn, I. J. Heo, I. S. Nam, J. H. Lee, Y. K. Youn and H. J. Kim, *Top. Catal.*, 2010, **53**, 57-63.
35. Z. Zhang, Y. Zhang, Z. Wang and X. Gao, *J. Catal.*, 2010, **271**, 12-21.
36. Z. Zhang, Y. Zhang, Q. Su, Z. Wang, Q. Li and X. Gao, *Environ. Sci. Technol.*, 2010, **44**, 8254-8258.
37. Y. Zhang, X. Wang, Z. Wang, Q. Li, Z. Zhang and L. Zhou, *Environ. Sci. Technol.*, 2012, **46**, 9614-9619.

38. Z. Wang, X. Yan, X. Bi, L. Wang, Z. Zhang, Z. Jiang, T. Xiao, A. Umar and Q. Wang, *Mater. Res. Bull.*, 2014, **51**, 119-127.
39. Q. Li, M. Meng, N. Tsubaki, X. G. Li, Z. Q. Li, Y. N. Xie, T. D. Hu and J. Zhang, *Appl. Catal. B*, 2009, **91**, 406-415.
40. Q. Li, M. Meng, H. Xian, N. Tsubaki, X. G. Li, Y. N. Xie, T. D. Hu and J. Zhang, *Environ. Sci. Technol.*, 2010, **44**, 4747-4752.
41. Q. Li, M. Meng, F. Dai, Y. Zha, Y. Xie, T. Hu and J. Zhang, *Chem. Eng. J.*, 2012, **184**, 106-112.
42. Z. Wang, Q. Li, L. Wang and W. Shangguan, *Appl. Clay Sci.*, 2012, **55**, 125-130.
43. A. E. Palomares, A. Uzcátegui and A. Corma, *Catal. Today*, 2008, **137**, 261-266.
44. L. Chmielarz, P. Kustrowski, A. Rafalska-Lasocha, D. Majda and R. Dziembaj, *Appl. Catal. B*, 2002, **35**, 195-210.
45. C. M. S. Polato, C. A. Henriques, A. C. C. Rodrigues and J. L. F. Monteiro, *Catal. Today*, 2008, **133**, 534-540.
46. Z. Jiang, J. J. Yu, J. Cheng, T. C. Xiao, M. O. Jones, Z. P. Hao and P. P. Edwards, *Fuel Process Technol.*, 2010, **91**, 97-102.
47. A. Pérez, M. Montes, R. Molina and S. Moreno, *Applied Catalysis A: General*, 2011, **408**, 96-104.
48. J. J. Yu, Z. Jiang, L. Zhu, Z. P. Hao and Z. P. Xu, *J. Phys. Chem. B*, 2006, **110**, 4291-4300.
49. Z. P. Wang, Z. Jiang and W. F. Shangguan, *Catal. Commun.*, 2007, **8**, 1659-1664.
50. E. Genty, R. Cousin, S. Capelle, C. Gennequin and S. Siffert, *Eur. J. Inorg. Chem.*, 2012, 2802-2811.
51. W.-P. Dow, Y.-P. Wang and T.-J. Huang, *Appl. Catal. A*, 2000, **190**, 25-34.
52. F. Kovanda, K. Jiratova, J. Rymes and D. Kolousek, *Appl. Clay Sci.*, 2001, **18**, 71-80.
53. M. Turco, G. Bagnasco, U. Costantino, F. Marmottini, T. Montanari, G. Ramis and G. Busca, *J. Catal.*, 2004, **228**, 43-55.
54. G. Fierro, M. Lo Jacono, M. Inversi, R. Dragone and P. Porta, *Top. Catal.*, 2000, **10**, 39-48.
55. I. Atribak, B. Azambre, A. Bueno López and A. García-García, *Appl. Catal. B*, 2009, **92**, 126-137.
56. S. Morandi, F. Prinetto, G. Ghiotti, M. Livi and A. Vaccari, *Micropor. Mesopor. Mat.*, 2008, **107**, 31-38.
57. G. Centi, G. E. Arena and S. Perathoner, *J. Catal.*, 2003, **216**, 443-454.
58. S. Roy and A. Baiker, *Chem. Rev.*, 2009, **109**, 4054-4091.
59. S. Wagloehner and S. Kureti, *Appl. Catal. B*, 2012, **125**, 158-165.
60. S. Wagloehner, M. Nitzer-Noski and S. Kureti, *Chem. Eng. J.*, 2015, **259**, 492-504.
61. Z. Wang, F. He, L. Wang, Z. Jiang, T. Xiao and Z. Zhang, *J. Nanosci. Nanotechno.*, 2014, **14**, 7087-7096.
62. Y. Zhang, Q. Su, Q. Li, Z. Wang, X. Gao and Z. Zhang, *Chem. Eng.Technol.*, 2011, **34**, 1864-1868.

Table 1. Chemical composition and structural parameters of the hydrotalcite precursors

Hydrotalcites Precursors	Compositions (molar ratio)	FWHM (2θ)	a (Å)	c (Å)	Xs (nm)	Weight loss (%) (total/first stage)
HT	Mg/Al=75/25	1.417	3.057	23.262	10.1	45.98/16.94
CuHT	Cu/Mg/Al=5/70/25	1.515	3.063	22.788	8.8	44.59/15.85
CoHT	Co/Mg/Al=5/70/25	1.572	3.067	23.308	9.3	45.70/17.70
CuCoHT	Cu/Co/Mg/Al=5/5/65/25	1.554	3.064	23.309	8.9	45.32/16.74

FWHM-Full width at half maximum of (003) plane;

Xs-Average crystallite size calculated from d(003) and d(110) planes using Debye-Scherrer equation;

Table 2. Textual properties and NO_x storage capacity of the oxide catalysts

Mixed Oxides	S_{BET}[a] (m^2/g)	Vp[b] (cm^3/g)	Dp[c] (nm)	H_2 uptake[d] (mmol/g)	NSC[e] (mg/g)
MgAl	186.2	0.88	18.9	0	2.66
CuMgAl	166.6	0.87	20.9	0.501	3.30
CoMgAl	185.4	0.83	18.0	0.094	5.20
CuCoMgAl	179.1	0.97	21.7	0.565	3.40

a-BET surface area, b-Total pore volume, c-Average pore size;

d-H_2 uptake at the range 100-500 °C in H_2-TPR tests ;

e-NOx storage capacity calculated from NOx-TPD tests

Table 3. Catalytic performance of Soot Combustion over the Oxides Catalysts

Samples	$C+O_2$			$C+NO+O_2$			
	T_5 (°C)	T_{50} (°C)	S_{CO2} (%)	T_5 (°C)	T_{50} (°C)	S_{CO2} (%)	C_m (%)
Blank	470	590	37.8	461	601	49.1	9.4
MgAl	422	577	70.9	320	563	88.3	17.2
CuMgAl	315	525	100	304	493	99.0	29.5
CoMgAl	344	528	100	330	486	99.1	25.3
CoCuMgAl	316	528	100	302	467	99.5	19.7

T_5 and T_{50} are defined as the temperatures at which 5% and 50% of the soot is converted, respectively;

S_{CO2}- selectivity to CO_2 formation; C_m-maximum conversion of NOx during soot oxidations

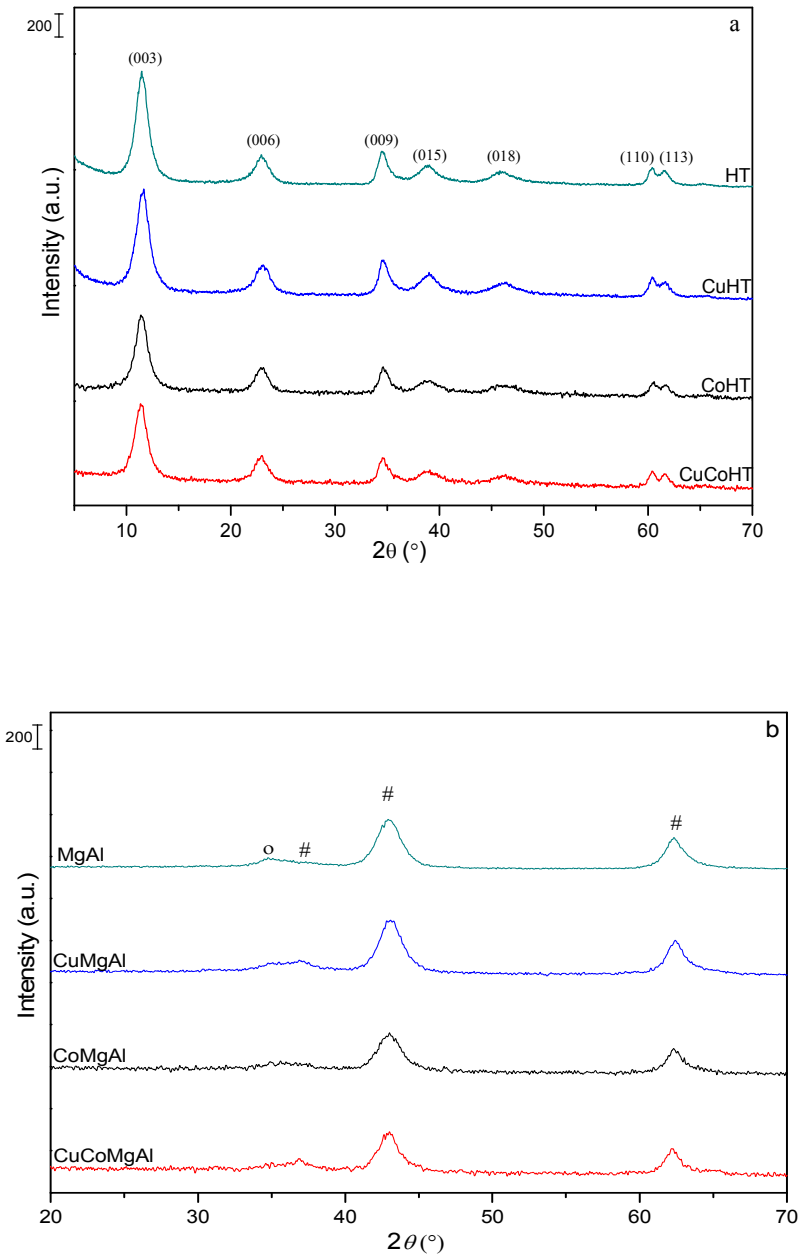

Figure 1. XRD patterns of hydrotalcite precursors (a) and calcined samples (b) (phases: #-the periclase-type MgO, o-the spinel-type $MgAl_2O_4$)

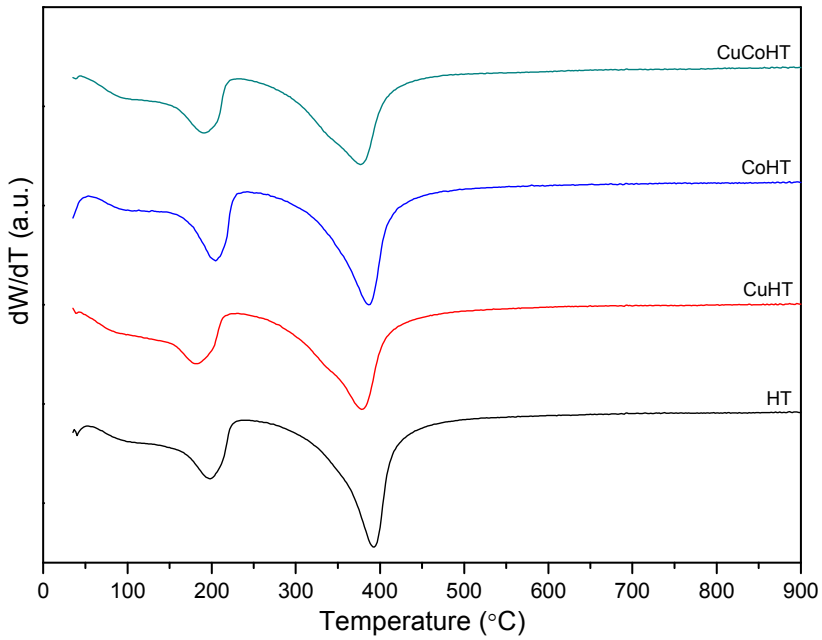

Figure 2. DTG curves of the as-synthesized hydrotalcite precursors.

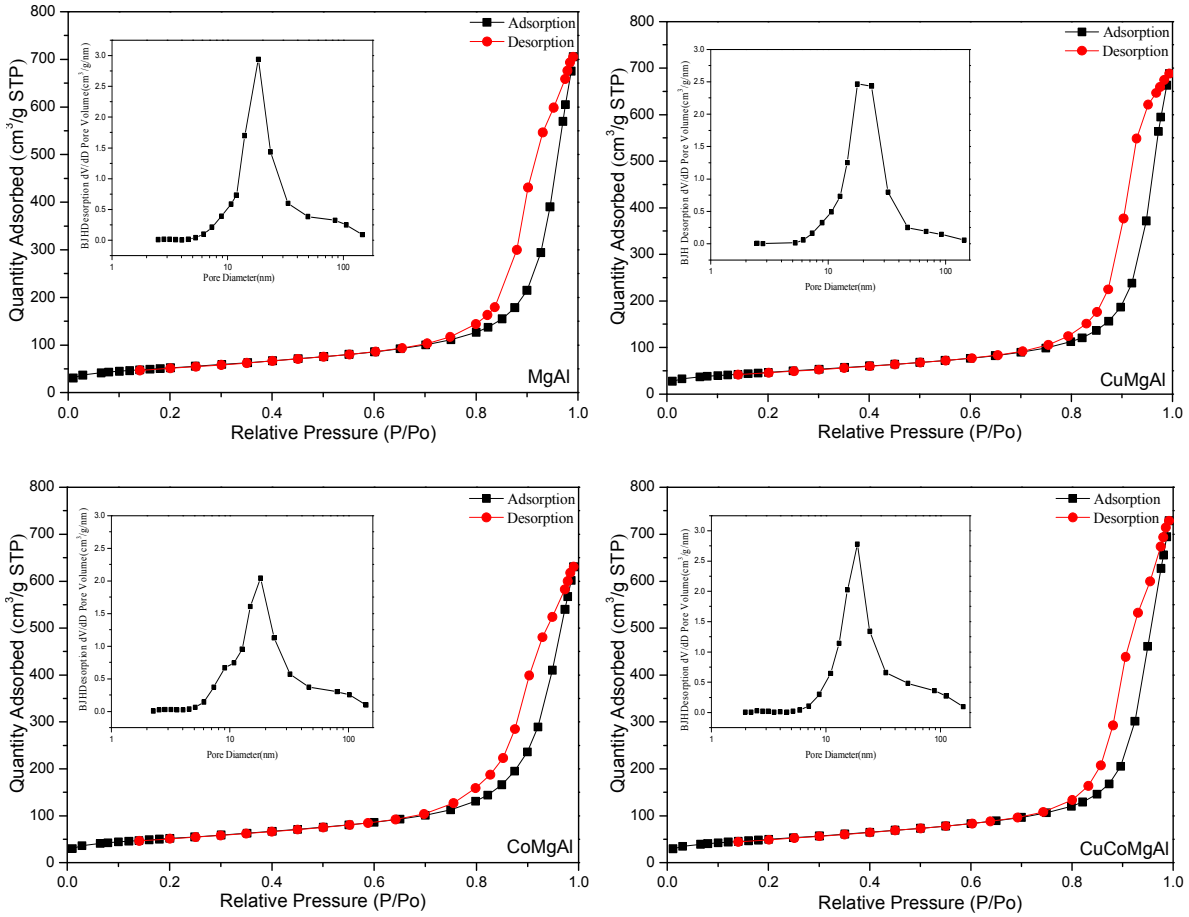

Figure 3. N_2 Adsorption and desorption isotherms of hydrotalcites-derived mixed oxides.

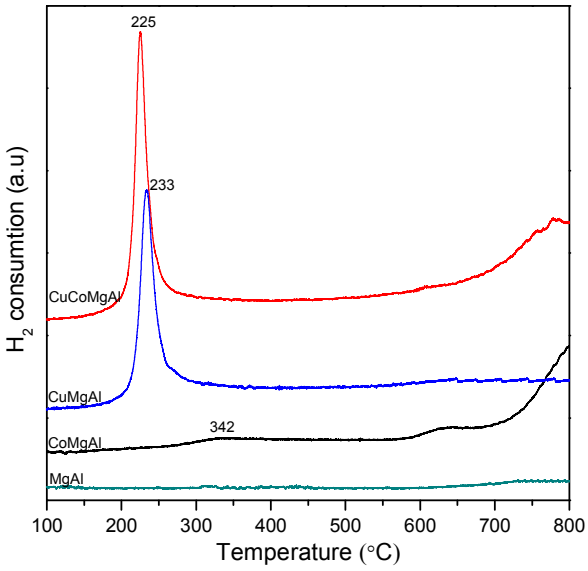

Figure 4. H_2-TPR patterns of mixed oxides samples

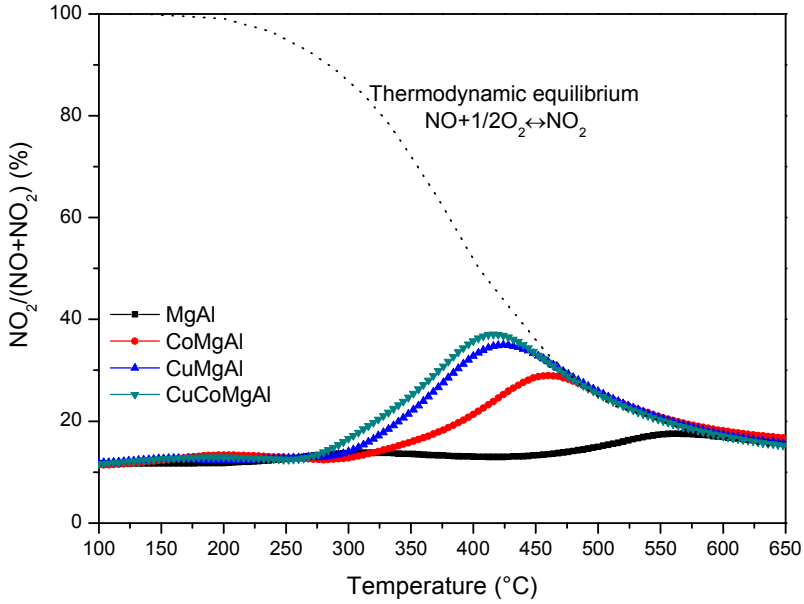

Figure 5. Catalyzed NO oxidation to NO_2 over the oxides samples

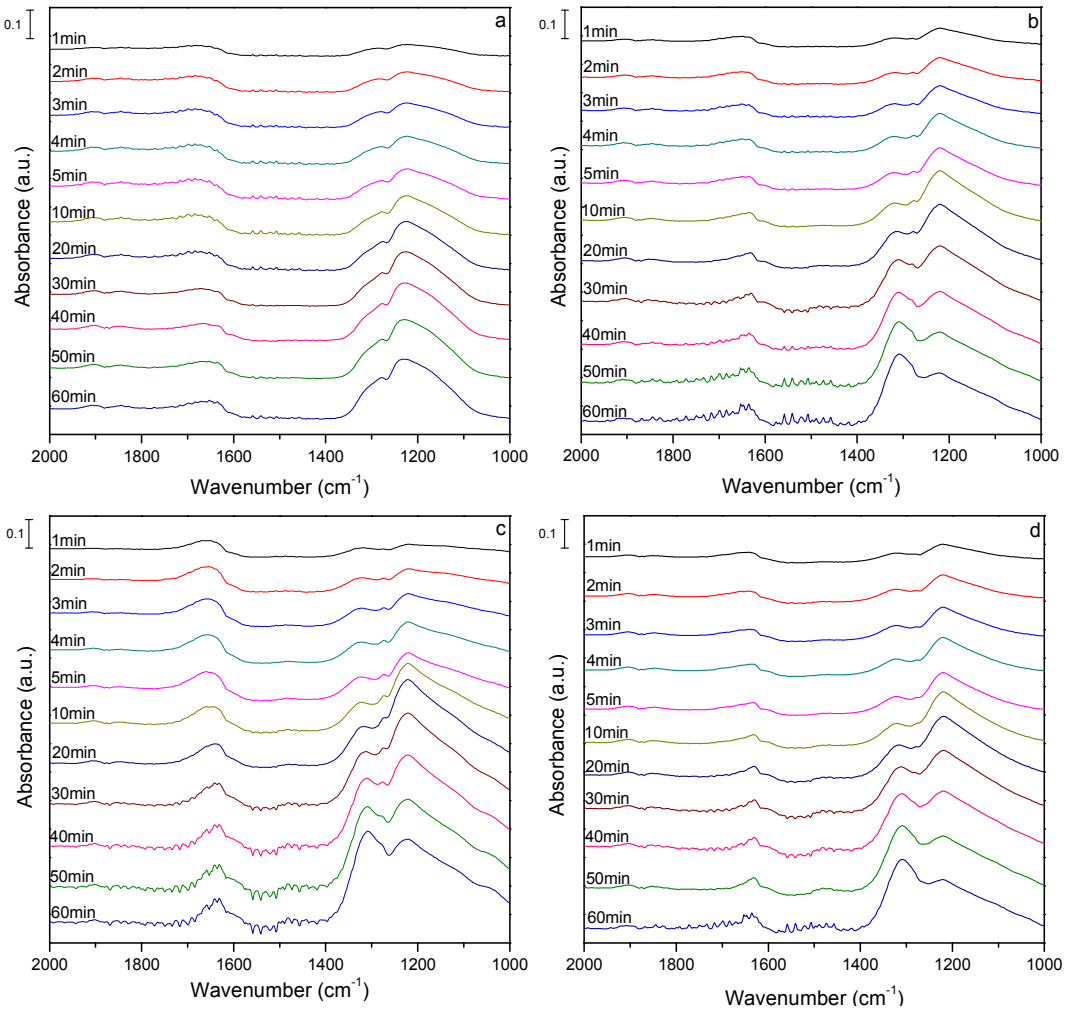

Figure 6. In situ IR spectra of NOx adsorption at 100°C over MgAl(a), CuMgAl(b), CoMgAl(c) and CuCoMgAl(d)

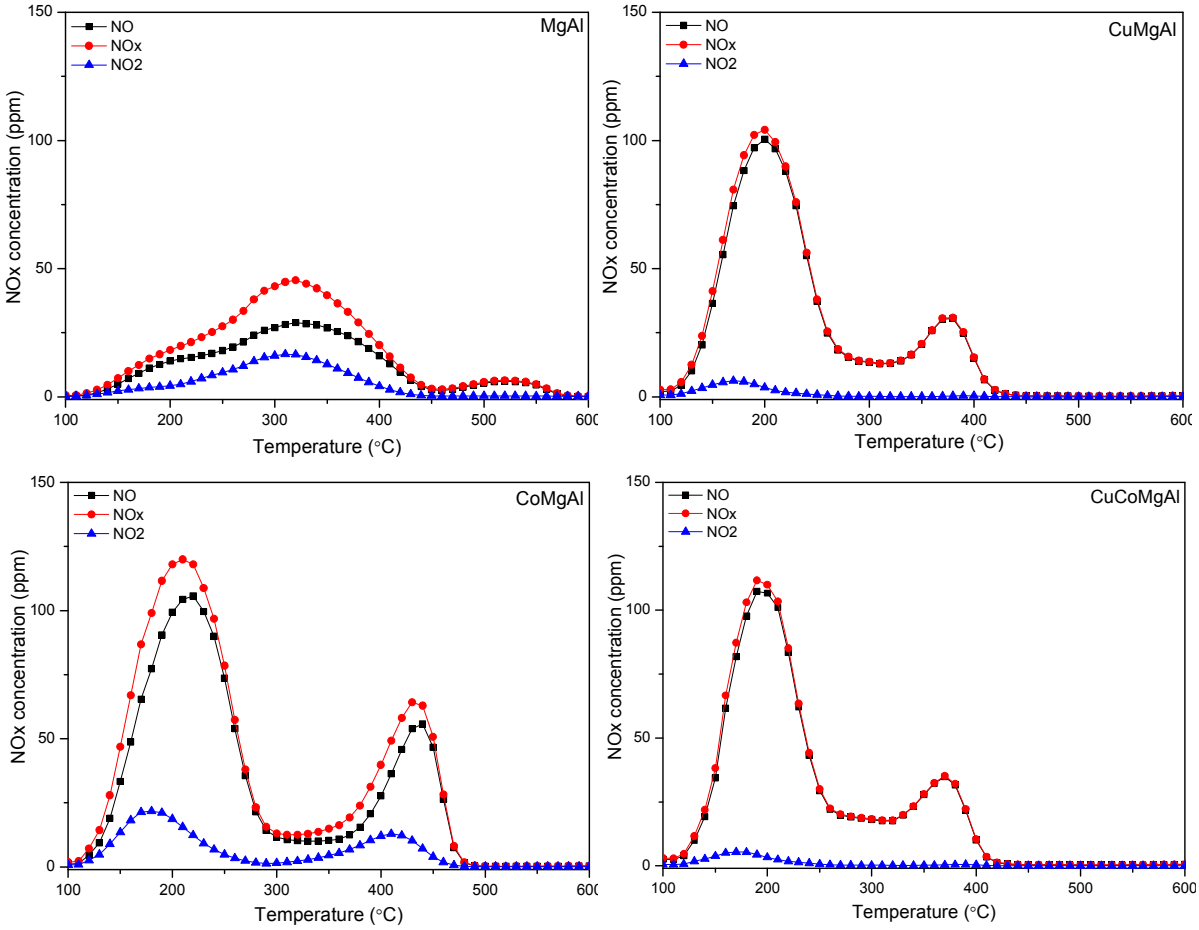

Figure 7. NO_x desorption profiles from the catalysts after the NOx adsorption at 100 ºC.

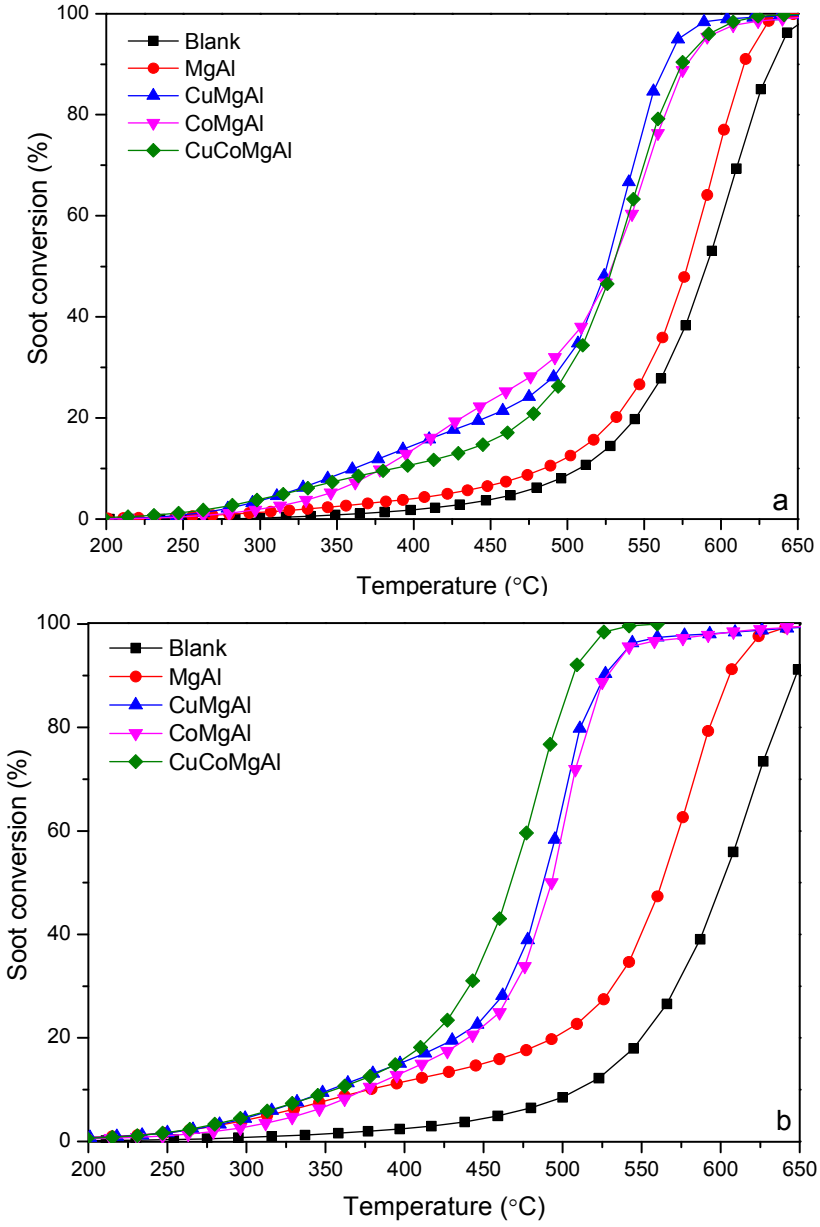

Figure 8. Catalytic oxidation of soot over hydrotalcites-derived mixed oxides in O_2 (a) and NO+O_2 (b).

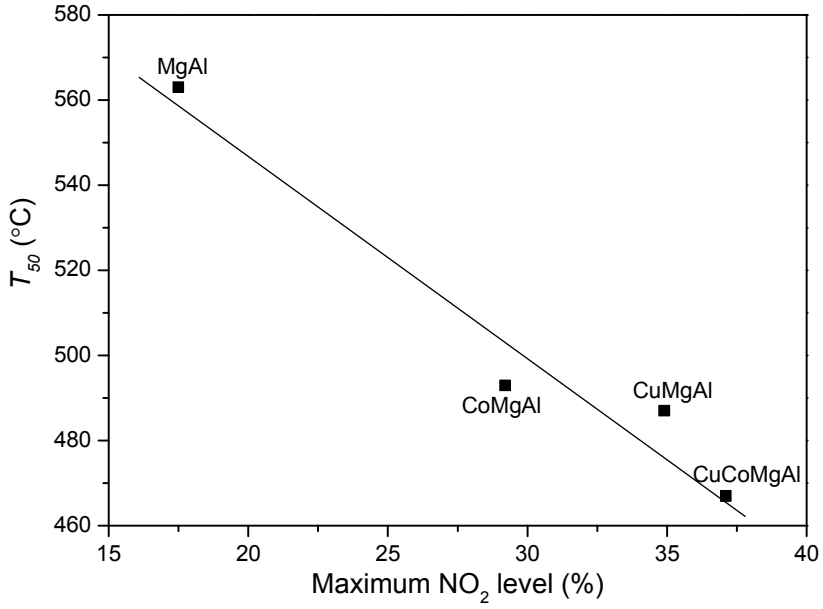

Figure 9. Relationship between mixed oxides-catalyzed NO oxidation to NO_2 and soot combustion (T_{50} parameter)